B-Site Cation-Induced Band Edge Shifts of Perovskite-Type $Cu(Nb,Ta)O_3$ Solid Solutions for Visible-Light-Driven Hydrogen Evolution

Haocong Wang,[a, c] Chihiro Takahashi,[a] Xuemeng Guo,[c] Shunya Okada,[a] Hajime Suzuki,[b] Daiming Tang,[d] Wei Yi,[a, ‡] Ikuya Yamada,[e] Xiaojuan Liu,[c] Ryu Abe,[b] and Koji Fujita[a, *]

[a]Department of Material Chemistry, Graduate School of Engineering, Kyoto University, Kyoto 615-8510, Japan
[b]Department of Energy and Hydrocarbon Chemistry, Graduate School of Engineering, Kyoto University, Kyoto 615-8510, Japan
[c]State Key Laboratory of Rare Earth Resource Utilization, Changchun Institute of Applied Chemistry, Chinese Academy of Sciences, Changchun 130022, China
[d]International Center for Materials Nanoarchitectonics (MANA), National Institute for Materials Science (NIMS), Tsukuba 305-0044, Japan
[e]Department of Materials Science, Graduate School of Engineering, Osaka Metropolitan University, Sakai, Osaka 599-8531, Japan

Abstract: The rational design of photocatalysts with precise bandgap and band-edge control is crucial for achieving the visible-light-driven conversion of solar to hydrogen. This study demonstrates a novel strategy for band-edge engineering through B-site cation substitution and symmetry evolution in Cu (d^{10})-based perovskites. Substitution of Ta^{5+} (d^0) for Nb^{5+} (d^0) in $CuNbO_3$ induces sequential phase transitions (Pc–$R3c$–$R\bar{3}c$), accompanied by systematic bandgap modulation from 1.57 to 2.23 eV. The $R\bar{3}c$ $CuTaO_3$ phase exhibits a much higher conduction band (−0.902 V vs SHE) than H^+/H_2 potential and a slightly lower valence band than O_2/H_2O potential. Visible-light-driven hydrogen evolution occurs efficiently on $CuTaO_3$ with Ru cocatalyst, in the presence of S^{2-}/SO_3^{2-} sacrificial agents. Our experiments and first-principles calculations reveal that the Ta-for-Nb-substitution widens the bandgap by lowering the valence band maximum via weakened Cu-O hybridization, while simultaneously elevating the conduction band minimum via Ta 5d orbital contributions. The inherent bandgap-narrowing tendency of structural evolution from polar Pc to centrosymmetric $R\bar{3}c$ symmetry is attenuated by Ta substitution-induced elongation of Cu-O bonds. The interplay between B-site cation engineering and symmetry-induced electronic degeneration establishes a materials design paradigm for visible-light-driven photocatalysis, demonstrating how to enable targeted bandgap optimization by coupling orbital-level modifications and phase transition.

1. INTRODUCTION

Photocatalytic water splitting is a promising method for the direct conversion of solar to hydrogen using particulate semiconductors. It is an environmentally clean process and only needs free and renewable solar energy, while fossil fuel-water reforming system requires continuous heat and releases a large amount of CO_2.[1,2] At present, the utilization of solar energy for photocatalytic water splitting is mainly concentrated in the ultraviolet region due to the wide bandgaps of semiconductors.[3–5] However, the content of ultraviolet light (300−400 nm) in the natural solar spectrum is too small to adequately harvest solar energy (less than 3%). Even if the apparent quantum yield is 100%, solar-to-hydrogen efficiency is limited to 1.7% in UV range.[3,6,7] In contrast, nearly 40% of sunlight is composed of visible light, which can also directly excite electrons and holes to drive water splitting. Hence, the practical solar hydrogen generation should focus on developing novel photocatalysts with narrow bandgap that enable them to split water efficiently under visible-light irradiation.

Oxide semiconductors have been continuously studied for photocatalytic water splitting due to their excellent stability. Up to now, numerous oxide photocatalysts could achieve overall water splitting with high efficiency, such as $SrTiO_3$ and $NaTaO_3$.[8–10] However, their bandgaps are so large that photoexcitation is strictly limited to UV irradiation. This is because the valence band maximum (VBM) is generally occupied by the stable but deep-lying O 2p orbitals, the level of which is about 3 eV, which is active for oxygen evolution reaction (OER).[11,12] When the conduction band minimum (CBM) is in a position where hydrogen evolution reaction (HER) can occur, visible-light response is completely impossible. So, a red-shift of bandgap is required to overcome this challenge. Building new VBM using other orbitals to effectively narrow bandgap could be a brilliant strategy for designing visible-light-driven HER photocatalysts.

In this context, oxides containing Cu^+ ions with a d^{10} electronic configuration have attracted much attention for valence band engineering, because the energy position of Cu 3d orbitals is more negative than that of O 2p orbitals.[11,13] In Cu^+ containing oxide semiconductors, valence band edge is composed of Cu 3d orbitals, allowing for narrow bandgap and visible-light absorption. For example, $LiNb_3O_8$ has a bandgap of 3.89 eV, which decreases significantly to 1.45 eV for $CuNb_3O_8$. In addition, their solid solution, $Li_{1-x}Cu_xNb_3O_8$, exhibits photocatalytic activity for hydrogen

generation under visible-light irradiation.[14] Similarly, the bandgap of $Cu_{3x}La_{1-x}Ta_7O_{19}$ solid solutions shows an obvious red-shift from 4.14 eV (x = 0) to 2.57 eV (x = 1).[15] Given the versatility and functionality of Cu_2O-Nb_2O_5 and Cu_2O-Ta_2O_5 systems where visible-light band gap size is observed due to a metal-to-metal charge transfer transition between filled Cu $3d^{10}$ and empty Nb/Ta $4d^0/5d^0$ bands, it is interesting to extend their compositional space to Cu_2O-richer regions such as $CuNbO_3$ and $CuTaO_3$ (50 mol% Cu_2O). $CuNbO_3$ crystallizes in a nonperovskite, $RbTaO_3$-type structure (space group $C2/m$) under ambient conditions, while perovskite-type monoclinic structure with space group Pc is stabilized by high-pressure synthesis.[16] $CuTaO_3$ cannot be obtained under ambient conditions, while the perovskite-related, polar rhombohedral structure with $R3c$ symmetry, which is often referred to as $LiNbO_3$-type structure, forms via high-pressure stabilization.[17] Nevertheless, the photocatalytic properties have not yet been reported for these high-pressure-synthesized perovskite and related compounds, i.e., $CuNbO_3$ and $CaTaO_3$, which will be hereafter denoted as HP-$CuNbO_3$ and HP-$CaTaO_3$, respectively.

Here, we target HP-$CuNbO_3$, HP-$CuTaO_3$, and their solid solutions HP-$Cu(Nb_{1-x}Ta_x)O_3$ and present a Ta substitution-assisted band edge engineering to construct new photocatalysts. Our structural analysis reveals that HP-$CuTaO_3$ adopts a nonpolar $R\bar{3}c$ structure at room temperature, unlike the polar $R3c$ structure as reported previously. We observe a Pc−$R3c$−$R\bar{3}c$ structure evolution by substituting Ta^{5+} for Nb^{5+} in the host lattice of HP-$CuNbO_3$. HP-$Cu(Nb_{1-x}Ta_x)O_3$ solid solutions respond to a large portion of visible light owing to their narrow bandgaps (1.57−2.23 eV). Notably, Ta substitution ultimately dominates the bandgap widening through elevating conduction band due to Ta 5d orbital contributions and lowering valence band by weakening Cu-O orbital hybridization. Particularly, $R\bar{3}c$ HP-$CuTaO_3$ exhibits a high HER overpotential (η_{HER}) and a small OER overpotential (η_{OER}), indicating that it is a promising visible-light-driven photocatalyst for hydrogen evolution in the presence of sacrificial agents.

2. EXPERIMENTAL SECTION

2.1 Synthesis and Characterization

$Cu(Nb_{1-x}Ta_x)O_3$ polycrystalline solid solutions (x = 0, 0.20, 0.35, 0.45, 0.75, and 1) were synthesized through the solid-phase reaction under high-pressure and high-temperature condition, as previously reported.[16] Cu_2O, Nb_2O_5, and Ta_2O_5 were used as the starting materials, and the stoichiometric mixture was pressed into a pellet and sealed in a capsule. $Cu(Nb_{1-x}Ta_x)O_3$ solid solutions (x = 0, 0.20, 0.35, 0.45, and 0.75) were prepared in a Ta capsule, and $CuTaO_3$ was prepared in a Pt capsule. The solid-state reaction was carried out in a Walker-type high-pressure device under 12 GPa at 1273 K. After being treated for 30 min, the temperature was quickly cooled to room temperature, followed by the slow release of the pressure. We tried to prepare one end member, $CuTaO_3$, under the same condition, 12 GPa and 1273 K, but an attempt to isolate it failed; a large amount of uncleared impurity phases was precipitated. The optimum condition was to treat the mixture in a pelletized from under a lower pressure (8 GPa) at 1273 K for 30 min.

Powder X-ray diffraction (XRD) patterns of products were initially recorded on a Rigaku SmartLab diffractometer (Cu Kα, λ = 1.5418 Å) to check the crystalline phase. For structural refinement, synchrotron XRD (SXRD) was performed at room temperature on the BL02B2 beamline at SPring-8 (λ = 0.775132 Å). Rietveld refinements were carried out through JANA2006[18] and FullProf.[19] X-ray absorption near edge structure (XANES) spectroscopy at Cu K-edge was collected in the transmission mode on the BL14B2 beamline at SPring-8. Optical second harmonic generation (SHG) response was measured using a pulsed Nd:YAG laser (EKSPLA, λ = 1064 nm; pulse duration, 25 ps; repetition frequency, 10 Hz) as the light source. The SHG light from the sample was detected with a photomultiplier tube through a 532 nm narrow band-pass filter.

Scanning electron microscopy (SEM) and transmission electron microscopy (TEM) with selected area electron diffraction (SAED) were used to characterize the morphology and microstructure. X-ray photoelectron spectroscopy (XPS) measurements were conducted using a MT-5500 system (ULVAC-PHI, Mg Kα). Photoelectron yield spectroscopy (PYS; BIP-KV201, Bunkoukeiki) was recorded to determine the ionization energy. UV−visible diffuse reflectance spectra (V-650, JASCO) were obtained to estimate the optical band gap energy.

2.2 Photocatalytic Reaction

Photocatalytic H_2 evolution over synthesized HP-$Cu(Nb_{1-x}Ta_x)O_3$ was conducted in a gas closed-circulation system using Ru nanoparticles as a cocatalyst and Na_2S-Na_2SO_3 as a sacrificial reagent. The photocatalyst powders (50 mg) were dispersed in aqueous solution (100 mL) containing Na_2S (0.1 mol L^{-1}) and Na_2SO_3 (0.5 mol L^{-1}) as sacrificial agents, with $RuCl_3 \cdot nH_2O$ (corresponding to 1 wt% as Ru metal) added to achieve 1 wt% Ru relative to the catalyst mass. In the initial stage of the reaction, photoexcited electrons reduced Ru^{3+} species, resulting in the *in-situ* deposition of Ru-based cocatalyst nanoparticles. The H_2 evolution reactions were performed under irradiation with a visible light (λ > 400 nm) by using an Xe lamp (Cermax, 300 W) equipped with an L-42 cutoff filter. The amounts of produced hydrogen were measured by gas

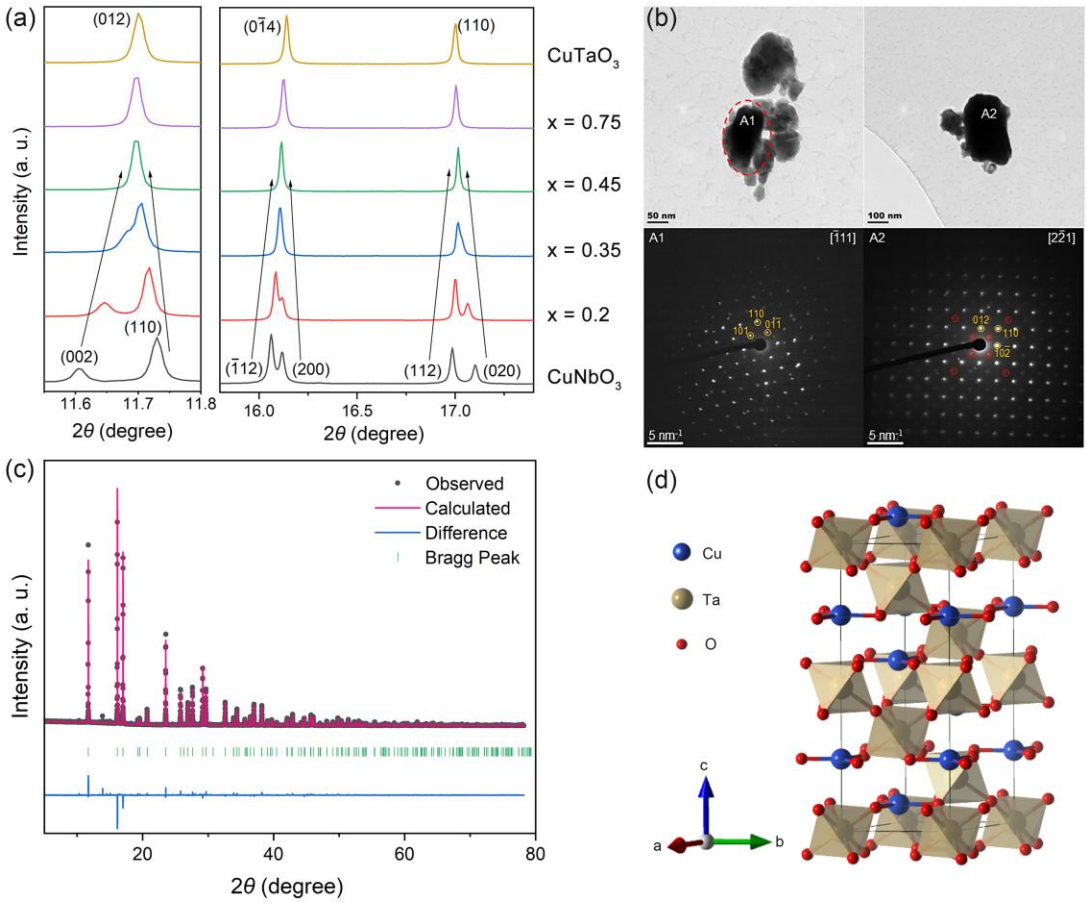

Figure 1. (a) SXRD patterns of $Cu(Nb_{1-x}Ta_x)O_3$ (x = 0, 0.2, 0.35, 0.45, 0.75, and 1) at room temperature (λ = 0.775132 Å). (b) TEM images and corresponding SAED patterns of $CuTaO_3$ in two different areas (A1 and A2). (c) Rietveld refinement against SXRD data (λ = 0.775132 Å) for $CuTaO_3$ at room temperature, and (d) refined crystal structure of $CuTaO_3$ ($R\bar{3}c$).

chromatography (GC-8A, Shimadzu, column: MS-5A, Ar carrier).

2.3 First-Principles Calculations

Within the framework of density functional theory (DFT), the electronic and crystal structures of $CuNbO_3$ and $CuTaO_3$ were calculated using the projection enhanced wave (PAW) method implemented in the Vienna ab-initio simulation package (VASP) code.[20–22] The cut-off energy of plane waves was set to 520 eV. All k-point grids used in the calculation were generated by the pre-post-data processing software VASPKIT.[23] The scattering pattern in Gamma format was chosen with a resolution of $2\pi \times 0.04$ Å^{-1} for k points in reciprocal space. The exchange-correlation functional was evaluated with the PBE functional.[24] An effective Hubbard parameter (U_{eff}) was considered based on Dudarev's approach.[25] In this study, we adopted U_{eff} = 2 eV and 3 eV for Pc and $R\bar{3}c$ phases, respectively, because the calculated bandgaps were close to the experimental results [see Supporting Information (SI) Table S1]. Using the PAW potentials, electrons taken to be valence are $3p^6 3d^{10} 4s^1$, $4s^2 4p^6 5s^2 4d^3$, $5p^6 6s^2 5d^3$, and $2s^2 2p^4$ for Cu, Nb, Ta, and O, respectively. The crystal structures were fully optimized until residual forces and stresses were less than 5.0×10^{-6} and 1.0×10^{-3} eV Å^{-1}, respectively. The crystal orbital Hamiltonian population (COHP) was calculated to investigate the covalent bond interactions between cations and oxide ions using the LOBSTER code.[26,27] The crystal structures were drawn using the VESTA code.[28]

3. RESULTS AND DISCUSSION

3.1 Crystal Structure and Valence States

In HP-$Cu(Nb_{1-x}Ta_x)O_3$ solid solution (x = 0, 0.20, 0.35, 0.45, 0.75, and 1), the one end member, HP-$CuNbO_3$, adopts an unusual polar structure with Pc symmetry, and possesses a "noncollinear ferrielectric" dipole order with weak polarity.[16] Here, we investigate the impacts of the Ta-substitution in HP-$CuNbO_3$ on the crystal structure. All samples were confirmed to be nearly single phase by laboratory XRD. SXRD data reveals that with increasing the Ta-for-Nb substitution x from 0 to 1, the splitting of 012, 01$\bar{4}$, and 110 peaks becomes smaller (blurred or indistinguishable) around x = 0.35 and disappear at $x \geq 0.45$ (Figure 1a and Figure S1). This indicates a structural phase

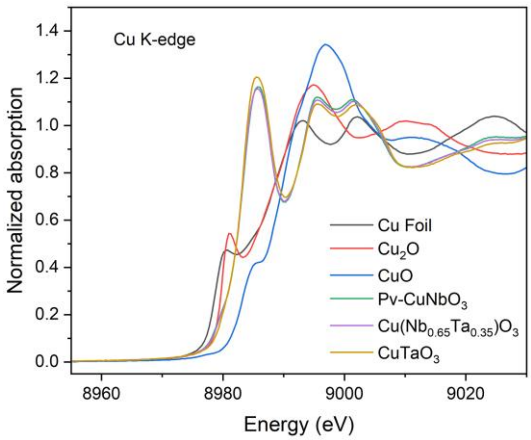

Figure 2. Experimental Cu K-edge XANES spectrum of $CuTaO_3$ (yellow) in comparison with those of Cu foil (black), Cu_2O (red), CuO (blue), Pv-$CuNbO_3$ (green),[16] and $Cu(Nb_{0.65}Ta_{0.35})O_3$ (purple).

transition of monoclinic to rhombohedral symmetry. Figure 1b shows selected area electron diffraction (SAED) patterns of HP-$CuTaO_3$ along $[\bar{1}11]$ and $[2\bar{2}1]$ zone axes. Note that the reflections marked with red circles are caused by double diffraction.[29,30] The reflection spots are consistent with the SXRD result and conform to the space groups $R3c$ or $R\bar{3}c$. The obvious difference is that the latter is centrosymmetric. To distinguish the space group uniquely, we checked the SHG activity of HP-$Cu(Nb_{1-x}Ta_x)O_3$ solid solutions ($0 \le x \le 1$). When the Ta-for-Nb substitution x is increased from 0 to 1, the SHG signal is observed up to x = 0.45 (Figure S2), whereas the SHG activity disappears in the range of $0.75 \le x \le 1$. This means that a phase transition takes place around x = 0.75 between noncentrosymmetric $R3c$ to centrosymmetric $R\bar{3}c$. The overall results demonstrate that the phase of $Cu(Nb_{1-x}Ta_x)O_3$ solid solutions ($0 \le x \le 1$) evolves from noncentrosymmetric Pc ($0 \le x \le 0.35$) to noncentrosymmetric $R3c$ (x = 0.45) and to centrosymmetric $R\bar{3}c$ ($0.75 \le x \le 1$).

For HP-$CuTaO_3$ (x = 1), Rietveld refinement was carried out against the SXRD data using the centrosymmetric $R\bar{3}c$ model as an initial structure, where Cu atoms are placed at 6a site (0, 0, 1/4), Ta atoms at 6b site (0, 0, 0), and O atoms at 18e site (x, 0, 1/4). Figure 1c shows that the stoichiometric composition model provides good overall fit to the observed pattern (profile R factor R_p = 4.27% and weighted profile R factor R_{wp} = 5.98%). We also consider the A-site splitting along the c-axis. Further, we examined the possibility of cation mixing at the 6a or 6b sites. In the previous structural analyses on $LiNbO_3$, the cation distribution was estimated to be $(Li_{1-5x}Nb_{x}\square_{4x})_A(Nb)_BO_3$ and $(Li_{1-5x}Nb_{5x})_A(Nb_{1-4x}\square_{4x})_BO_3$, where □ represents a vacancy.[31,32] In the course of our refinement against SXRD data, we considered two models, $(Cu_{1-x}Ta_x)_A(Ta_{1-x}\square_x)_BO_3$ and $(Cu_{1-x}\square_x)_A(Cu_xTa_{1-x})_BO_3$, but the introduction of a small degree of cation mixing (a few

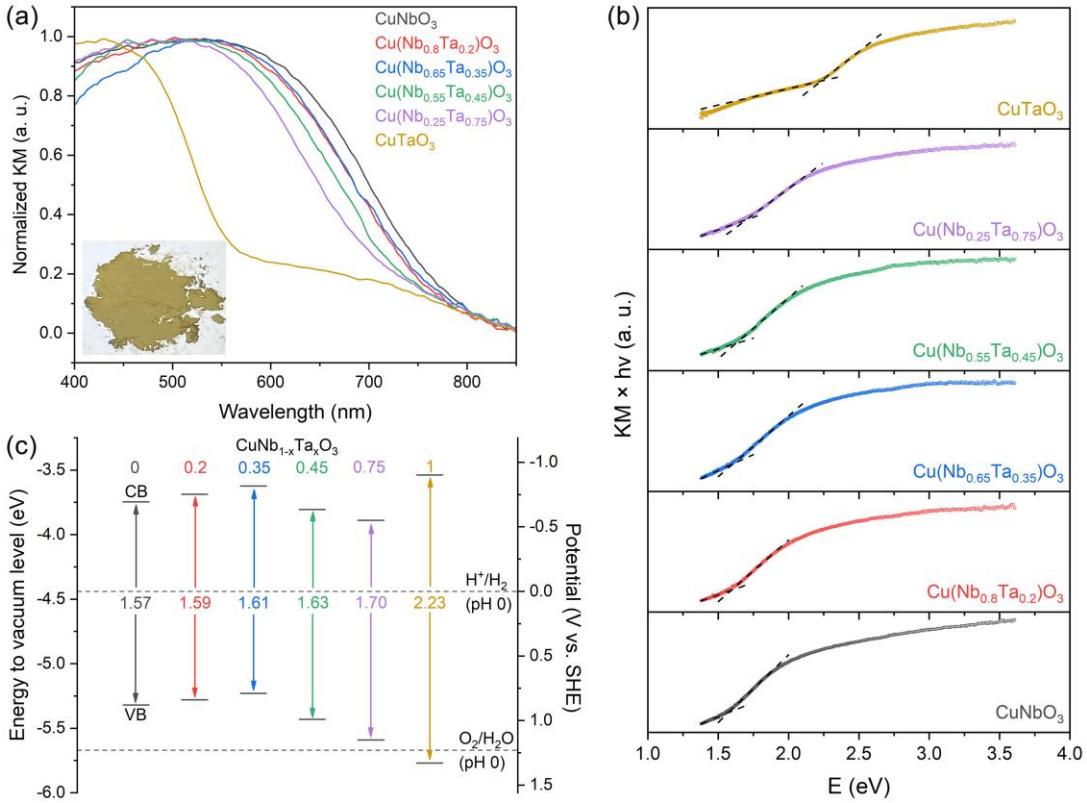

Figure 3. (a) UV−vis diffuse reflectance spectra and photograph of $CuTaO_3$, (b) converted Tauc plots, and (c) schematic band structure diagram.

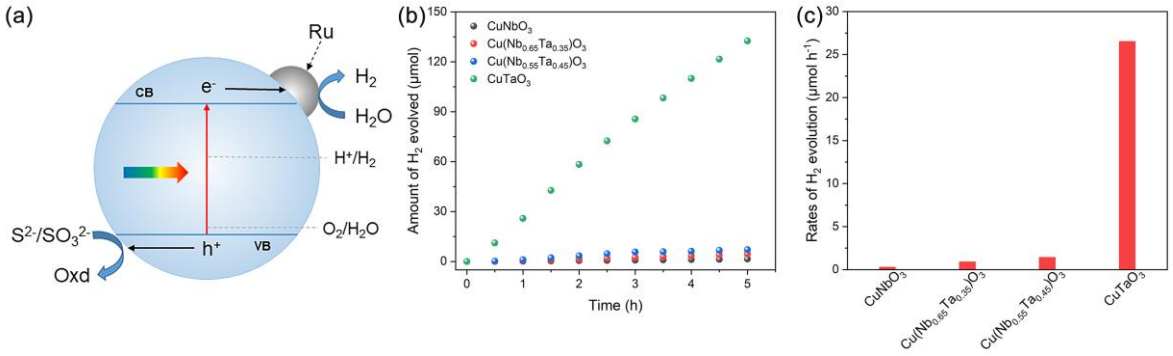

Figure 4. (a) Illustration of photocatalytic reaction over the Ru/HP-$CuTaO_3$ photocatalyst. (b) Time course of H_2 production from water containing Na_2S (0.1 M) and Na_2SO_3 (0.5 M) under visible-light irradiation (λ > 400 nm), and (c) corresponding H_2 production rates.

percent) at the 6a or 6b sites did not improve the fitting quality. The final refined crystal structure with a model without A-site splitting and cation mixing is displayed in Figure 1d, and the structural parameters are listed in Table S2. Bond-valence-sum calculations[33] using the SXRD-refined bond lengths give +0.858(3) and +5.038(11) for Cu and Ta, respectively, confirming the $Cu^{+}Ta^{5+}O_3$ ionic model.

Figure 2 shows the XANES spectra at Cu K-edge of HP-$CuNbO_3$, HP-$Cu(Nb_{0.65}Ta_{0.35})O_3$, HP-$CuTaO_3$, and reference materials, which can give us details about the valence state and coordination environment of Cu. The Cu K-edge XANES spectra of HP-$CuTaO_3$, HP-$CuNbO_3$, and HP-$Cu(Nb_{0.65}Ta_{0.35})O_3$ are very similar to each other. Their absorption edge positions are close to that of Cu_2O, but different from that of CuO. Nevertheless, the contrasting coordination environment between high-pressure-synthesized Cu oxides and Cu_2O (linear coordination) makes it difficult to estimate the Cu valency from the spectral comparison. In our previous work of HP-$CuNbO_3$,[16] its Cu K-edge XANES experimental spectrum matches qualitatively the calculated spectrum based on a $Cu^{+}Nb^{5+}O_3$ model, demonstrating that the Cu cations are present as Cu^{+}. In this context, the Cu valency of HP-$CuTaO_3$ and HP-$Cu(Nb_{0.65}Ta_{0.35})O_3$ can be easily estimated to be +1 from the similarity of their experimental spectra to that of HP-$CuNbO_3$, which validates the result obtained by BVS calculations. Thus, it is reasonable to conclude that the formal valence state of Nb/Ta in HP-$Cu(Nb,Ta)O_3$ is +5.

3.2 Optical Property and Band Structure

The optical properties of HP-$Cu(Nb_{1-x}Ta_x)O_3$ solid solutions (x = 0, 0.20, 0.35, 0.45, 0.75, and 1) were investigated by UV-vis diffuse reflectance spectra. The results are shown in Figure 3a. All samples display obvious visible-light absorption, suggesting the characteristics of narrow bandgap. This feature is relevant to the involvement of Cu 3d orbitals to valence band, which gives rise to the bandgap excitation into the empty Nb/Ta $4d^0/5d^0$ conduction bands. With the increase in Ta-for-Nb substitution x, the absorption edge gradually shifts to the shorter wavelength side, indicating that bandgap becomes wider. This is because the energy level of Ta 5d orbitals is higher than that of Nb 4d orbitals. Namely, the conduction band shifts upward through Ta substitution. A similar phenomenon has been observed in other Nb-Ta solid-solution systems.[34–37] The bandgap estimated by the Tauc plot converted from the diffuse reflection spectrum gradually increases from 1.57 eV for HP-$CuNbO_3$ to 2.23 eV for HP-$CuTaO_3$ (Figure 3b). In this study, we evaluated the energy levels of the valence band maximum (VBM) from their ionization energies measured by PYS (Figure S3).[38,39] The energy level of the conduction band minimum (CBM) was also determined by adding the band gap energy to the VBM level. The proposed band structures are presented in Figure 3c. In this figure, the electrode potential versus standard hydrogen electrode (SHE) is also shown on the right axis.[40] One can see that HP-$Cu(Nb_{1-x}Ta_x)O_3$ solid solutions ($0 \leq x \leq 1$) possess more negative CBM than the reduction potential of H^{+}/H_2, indicating that they can in principle meet the thermodynamic requirements for photocatalytic H_2 evolution. Notably, HP-$CuTaO_3$ (x = 1) shows a slightly positive valence band (VB) potential (E_{VB}, +1.33 V vs SHE) as compared to the oxidation potential of O_2/H_2O, and its conduction band (CB) potential (E_{CB}, −0.902 V vs SHE) is superior to those of other compounds. Thus, HP-$CuTaO_3$ can be regarded as a promising photocatalyst for H_2 evolution.

3.3 Photocatalytic Activity

With the aid of Ru cocatalyst, several representative materials are selected to evaluate the photocatalytic performance of hydrogen evolution reaction in an aqueous Na_2S-Na_2SO_3 solution under visible-light irradiation (λ > 400 nm). All samples are characterized by an assembly of particles as large as 1−2 μm without significant differences in morphology (Figure S4). Figure 4a illustrates the charge transport process and subsequent surface reaction over the Ru/HP-$CuTaO_3$ photocatalyst. Figure 4b and 4c shows the photocatalytic HER activity of HP-$Cu(Nb_{1-x}Ta_x)O_3$. Owing

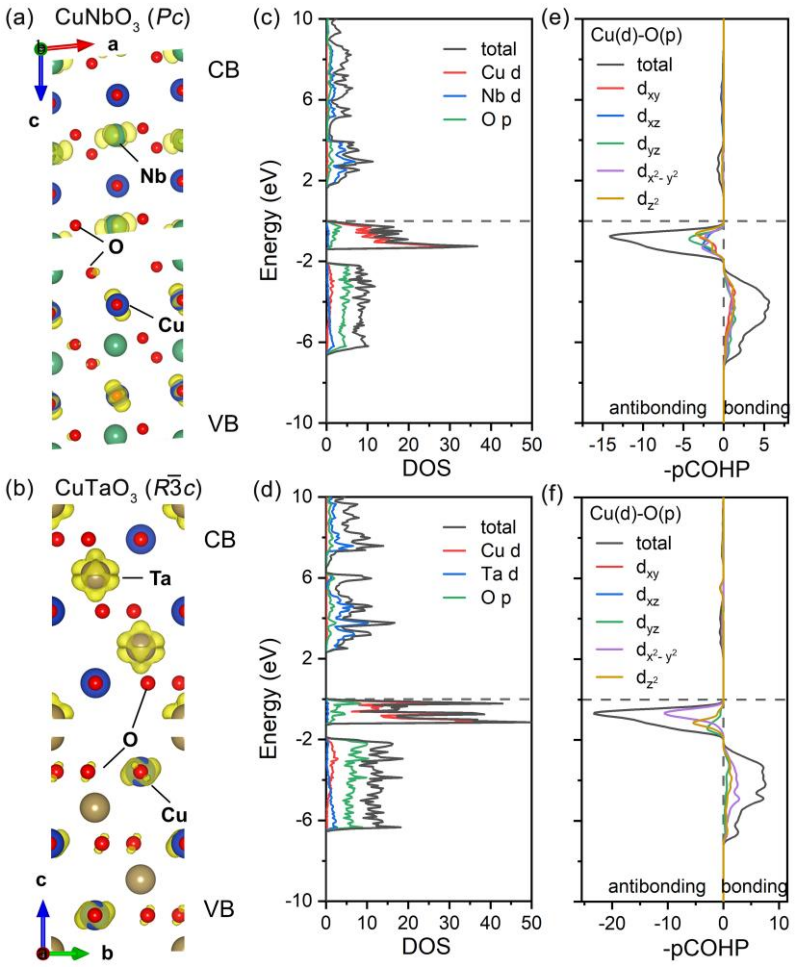

Figure 5. (a, b) Charge density distribution of the valence band (VB) and conduction band (CB), (c, d) projected electronic density of states (DOS), and (e, f) crystal orbital Hamilton population (COHP) for *Pc* $CuNbO_3$ and $R\bar{3}c$ $CuTaO_3$.

to the increase in reduction potential E_{CB} (Figure 3c), $Cu(Nb_{0.65}Ta_{0.35})O_3$ shows a higher H_2 production rate (0.9 μmol h^{-1}) than does $CuNbO_3$ (0.3 μmol h^{-1}). The H_2 evolution rate of $Cu(Nb_{0.55}Ta_{0.45})O_3$ reaches 1.4 μmol h^{-1}. The improvement of photocatalytic activity is probably caused by the structural transformation from weakly polar *Pc* phase into strongly polar *R*3*c* phase (Figure 1). It is well known that the charge transport process is crucial to the kinetics of subsequent surface reactions. In polar structures, local electric field can provide a driving force for the separation of photo-generated electrons and holes and thus prevent the charge recombination.[41–43] Remarkably, HP-$CuTaO_3$ shows an excellent H_2 evolution rate of 26.5 μmol h^{-1}, which is much higher than the those for HP-$Cu(Nb,Ta)O_3$ and HP-$CuNbO_3$ (Figure 4c). The obviously negative shift of conduction band (E_{CB}) provides highly active electrons for photocatalytic H_2 evolution. Meanwhile, the redox potentials S^{2-}/SO_3^{2-} are so negative that they can consume photogenerated positive holes and prevent charges recombination efficiently.[44–46] The rapid depletion of positive holes is conducive to the separation and transfer of photoelectrons and leads to a higher hydrogen evolution rate. Moreover, Ru cocatalyst distributes on the surface of photocatalyst and acts as an electron collector.[47] It has been proved that the strongly coupled heterostructure interface induces a unique interfacial interpenetration effect that optimizes the adsorption of intermediates, leading to excellent catalytic activity for hydrogen evolution in alkaline media.[48] Therefore, the interfacial interaction of Ru and HP-$CuTaO_3$ may play a vital role in the photocatalytic HER activity.

We also examine the stability of the present Cu^+-containing compounds during the photocatalytic reactions. The XRD measurements reveal that the photostability and water stability are high (Figure S5). This is a characteristic of Cu^+-containing complex oxides, unlike Cu_2O.[49–51] Additionally, we performed XPS to check the valence states of Cu at the surface of samples before and after light irradiation (Figure S6). Two couples of peaks at 933.7 and 953.8 eV are obtained for Cu $2p_{3/2}$ and Cu $2p_{1/2}$, respectively.[52,53] The Cu $2p_{3/2}$ component has two main peaks at ~933 eV (Cu^+) and ~935 eV (Cu^{2+}).[54,55] Besides of

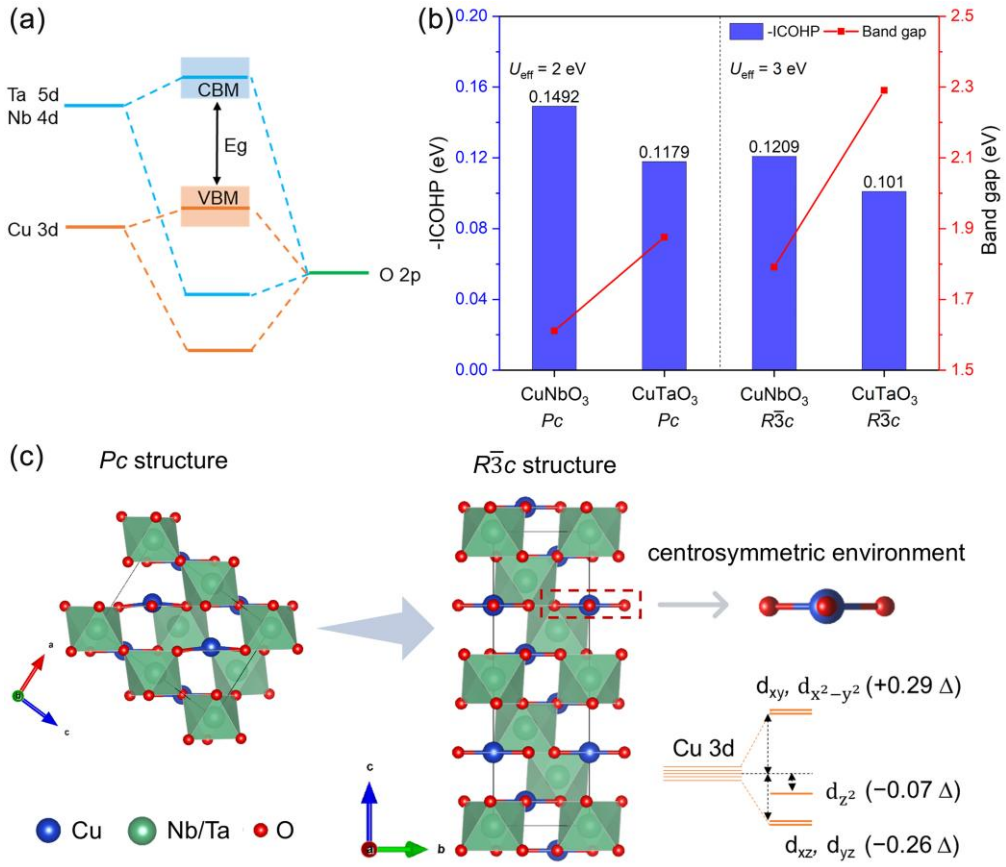

Figure 6. (a) Energy level diagram of the d-p interactions in $CuNbO_3$ and $CuTaO_3$, (b) the effect of symmetry transition on d orbitals splitting, and (c) the –ICOHP and corresponding band gap of Ta-substituted $CuNbO_3$.

these, Cu $2p_{3/2}$ spectra show the shakeup satellite peaks at ~943 and ~945 eV, corresponding to Cu^{2+} and Cu^{+}, respectively.[56] For the Cu $2p_{1/2}$ component, the two main peaks at ~953 eV (Cu^{+}) and ~955 eV (Cu^{2+}) are observed, along with their shakeup satellite (~963 eV). Therefore, the mixed valence states of Cu^{+}/Cu^{2+} coexist in the surface of the as-prepared samples. XPS results demonstrate that when the powders are dispersed in an aqueous Na_2S-Na_2SO_3 solution without light irradiation, Cu^{2+} is almost reduced to Cu^{+} due to the high reducibility of S^{2-}/SO_3^{2-}. The monovalent state of copper ions remains after photocatalytic process (Figure S6). Consequently, the surface state of Cu is close to the bulk valence by using sulfur-based sacrificial agents, which has a positive effect for the separation and transfer of photoelectrons.

3.4. Energy Band Calculations

To elucidate the origin of Ta substitution-induced band edge shifts (Figure 3c), we systematically analyzed the electronic band structures in HP-$Cu(Nb_{1-x}Ta_x)O_3$ system using DFT calculations. The calculated bandgaps agree well with experimental values when employing U_{eff} = 2 eV for *Pc* $CuNbO_3$ and U_{eff} = 3 eV for $R\bar{3}c$ $CuTaO_3$, respectively (Table S1). To decouple the concurrent effects of B-site cation substitution (of Ta for Nb) and structural symmetry evolution (from *Pc* to $R\bar{3}c$) on the band gap widening from *Pc* $CuNbO_3$ (1.57 eV) to $R\bar{3}c$ $CuTaO_3$ (2.23 eV), hypothetical intermediate-member structures, *Pc* $CuTaO_3$ and $R\bar{3}c$ $CuNbO_3$, were computationally modeled for comparative analysis.

Charge density distributions and the projected electronic density of states (DOS) demonstrate that the conduction bands in *Pc* and $R\bar{3}c$ $CuMO_3$ (*M* = Nb and Ta) predominantly comprise Nb 4d (for *M* = Nb) or Ta 5d (for *M* = Ta) orbitals hybridized with O 2p orbitals, while the valence bands arise primarily from O 2p and Cu 3d orbital interactions (Figure 5a-d, S7-S8). Crystal orbital Hamilton population (COHP) analysis proves that Cu-O antibonding orbitals contribute VBM (Figure 5e-5f and S9). Therefore, bandgap is governed by the antibonding Cu-O (VBM) and Nb/Ta-O (CBM) interactions (Figure 6a).

To reveal the origin of bandgap widening, absolute VBM and CBM positions for *Pc* and $R\bar{3}c$ $CuMO_3$ (*M* = Nb and Ta) were calculated via the Mulliken electronegativity method (Figure S10).[57] Notably, Ta substitution induces significant CBM upshift through replacement of Nb 4d orbitals by higher-energy Ta 5d orbitals. COHP calculations further

demonstrate weakened Cu-O covalent interactions in Ta-substituted phases, as evidenced by reduced −ICOHP (integrated COHP) values (Figure 6b). This diminished orbital hybridization simultaneously lowers VBM energy while elevating CBM through Ta 5d orbital contributions. The reduction in orbital overlaps is further supported by bond length elongation in Ta-substituted phases (Table S3). Therefore, the B-site cation substitution-induced Cu-O bond elongation is regarded as a dominant factor in modulating electronic properties across *Pc* and $R\bar{3}c$ structures (Figure 6b and S10).

It should be mentioned that the structural evolution from polar *Pc* to centrosymmetric $R\bar{3}c$ symmetry induces distinct crystal field splitting of Cu 3d orbitals (Figure 6c). In the $R\bar{3}c$ phase, trigonal planer coordination environment splits Cu^{+} d-orbitals into doubly degenerate (d_{xz}, d_{yz}), nondegenerate (d_{z^2}), and doubly degenerated (d_{xy}, $d_{x^2-y^2}$) states (Figure S11a and S11b). In contrast, the distorted *Pc* Cu*M*O_3 structure lacks such symmetry-driven degeneracy (Figure S11c and S11d). The enhanced crystal field splitting in $R\bar{3}c$ phase raises the energy of Cu-O antibonding orbitals, potentially narrowing bandgaps through VBM upshifting (Table S1 and Figure S10). This trend aligns with the prior studies on Ag-based perovskites (e.g., $AgNbO_3$, $AgTaO_3$), emphasizing the critical role of A-site coordination effects on d-orbital energetics.[58] However, our experimental observations of HP-Cu($Nb_{1-x}Ta_x$)O_3 contradict this trend, as the dominant influence of Ta substitution overrides the symmetry-driven effects. The attenuated Cu-O hybridization reduces VBM upshift while amplifying Ta-induced CBM elevation, collectively contributing to the observed bandgap widening (Figure 6b). Therefore, this counterintuitive behavior between experimental observations and symmetry-driven trend highlights the Ta substitution-induced modulation of both band edges through reduced O 2p-Cu 3d hybridization at VBM and enhanced Ta 5d-O 2p antibonding interactions at CBM.

These computational insights demonstrate the critical interplay between B-site cations engineering and structural symmetry in modulating band structures. The bond strength variation with Ta substitution, as a dominant factor, overrides the symmetry-driven trends and ultimately governs the band edge shifts. This dual-control mechanism provides a strategic pathway for precise band structure tuning in oxide photocatalysts.

4. CONCLUSIONS

This work demonstrates that perovskite related oxides, Cu(Nb,Ta)O_3, show photocatalytic activity for hydrogen evolution under visible-light irradiation. These compounds are obtained as the metastable phases by means of high-pressure synthesis. The substitution of Ta^{5+} for Nb^{5+} in $CuNbO_3$ leads to a phase transition from *Pc* to *R*3*c* to $R\bar{3}c$. In our study, the crystal symmetry of $CuTaO_3$ is ascribed to a nonpolar rhombohedral $R\bar{3}c$, unlike a polar rhombohedral *R*3*c* ($LiNbO_3$-type structure) as reported previously.[17] The bandgap widens from 1.57 to 2.23 eV with increasing the Ta substitution. Combined with theoretical analyses, we demonstrate that Ta substitution dominantly governs band edge shifts by simultaneously elevating the CBM via Ta 5d orbital contributions and lowering the VBM though attenuated Cu-O hybridization. While structural symmetry evolution (*Pc* to $R\bar{3}c$) inherently promotes bandgap narrowing via enhanced crystal field splitting, these symmetry mediated effects are overridden by Ta-induced electronic perturbations. These findings provide a generalizable strategy for designing visible-light-responsive photocatalysts through targeted d-orbital modulation and coordination engineering.

ASSOCIATED CONTENT

Supporting Information

The Supporting Information is available free of charge on the ACS Publications website at DOI:

Additional SXRD analyses, first-principles calculations results, SEM images, and SHG data and XPS results

CONFLICTS OF INTEREST

There are no conflicts to declare.

AUTHOR INFORMATION

Corresponding Author

‡ yi.wei.5c@kyoto-u.ac.jp
* fujita.koji.5w@kyoto-u.ac.jp

ACKNOWLEDGMENT

This work was supported by JSPS Postdoctoral Fellowships for Research in Japan (Grant Number F21750), the Grant-in-Aid for the JSPS KAKENHI (Grant Numbers JP21H04619, JP22F21750, JP22K04686, and JP22H01775, and 24K21688), the JSPS Research Fellow (Grant Number 22KF0195), and the "Advanced Research Infrastructure for Materials and Nanotechnology in Japan (ARIM)" of the MEXT (Proposal Number JPMXP1222HK0061). K. F. acknowledges grants from the Murata Science Foundation, the lketani Science and Technology Foundation, the Nippon Sheet Glass Foundation for Materials Science and Engineering, the Mitsubishi Foundation, the Okura Kazuchika Memorial Foundation, Izumi Science and Technology Foundation, and JFE 21 Century Foundation. SXRD experiments were performed on BL02B2 at SPring-8 with the approval of JASRI (Proposal Nos. 2022A1587, 2022B0553, 2022B1668, 2023A1498, and 2024A1510).

REFERENCES

(1) Shaner, M. R.; Atwater, H. A.; Lewis, N. S.; McFarland, E. W. A Comparative Technoeconomic Analysis of Renewable Hydrogen Production Using Solar Energy. *Energy Environ. Sci.* **2016**, *9*, 2354–2371.

(2) Wang, Q.; Nakabayashi, M.; Hisatomi, T.; Sun, S.; Akiyama, S.; Wang, Z.; Pan, Z.; Xiao, X.; Watanabe, T.; Yamada, T.; Shibata, N.; Takata, T.; Domen, K. Oxysulfide Photocatalyst for Visible-Light-Driven Overall Water Splitting. *Nat. Mater.* **2019**, *18*, 827–832.

(3) Takata, T.; Jiang, J.; Sakata, Y.; Nakabayashi, M.; Shibata, N.; Nandal, V.; Seki, K.; Hisatomi, T.; Domen, K. Photocatalytic Water Splitting with a Quantum Efficiency of Almost Unity. *Nature* **2020**, *581*, 411–414.

(4) Qin, Y.; Fang, F.; Xie, Z.; Lin, H.; Zhang, K.; Yu, X.; Chang, K. La,Al-Codoped $SrTiO_3$ as a Photocatalyst in Overall Water Splitting: Significant Surface Engineering Effects on Defect Engineering. *ACS Catal.* **2021**, *11*, 11429–11439.

(5) Fujishima A, H. K. Electrochemical Photolysis of Water at a Semiconductor Electrode. *Nature* **1972**, *238*, 37–38.

(6) Hisatomi, T.; Takanabe, K.; Domen, K. Photocatalytic Water-Splitting Reaction from Catalytic and Kinetic Perspectives. *Catal. Lett.* **2015**, *145*, 95–108.

(7) Zhou, P.; Navid, I. A.; Ma, Y.; Xiao, Y.; Wang, P.; Ye, Z.; Zhou, B.; Sun, K.; Mi, Z. Solar-to-Hydrogen Efficiency of More than 9% in Photocatalytic Water Splitting. *Nature* **2023**, *613*, 66–70.

(8) Domen K.; B.; Naito, S.; Soma, M.; Onishi, T.; Tamaru, K. Photocatalytic Decomposition of Water Vapour on an NiO-$SrTiO_3$ Catalyst. J.C.S. Chem. Comm. **1980**, *12*, 543–544.

(9) Kato, H.; Kudo, A. Highly Efficient Decomposition of Pure Water into H_2 and O_2 over $NaTaO_3$ Photocatalysts. *Catal. Lett.* **1999**, *58*, 153–155.

(10) Mai, H.; Chen, D.; Tachibana, Y.; Suzuki, H.; Abe, R.; Caruso, R. A. Developing Sustainable, High-Performance Perovskites in Photocatalysis: Design Strategies and Applications. *Chem. Soc. Rev.* **2021**, *50*, 13692–13729.

(11) Kudo, A.; Miseki, Y. Heterogeneous Photocatalyst Materials for Water Splitting. *Chem. Soc. Rev.* **2009**, *38*, 253–278.

(12) D.E. Scaife. Oxide Semiconductors in Photoelectrochemical Conversion of Solar Energy. *Solar Energy* **1980**, *25*, 41–54.

(13) Hisatomi, T.; Domen, K. Reaction Systems for Solar Hydrogen Production via Water Splitting with Particulate Semiconductor Photocatalysts. *Nat. Catal.* **2019**, *2*, 387–399.

(14) Sahoo, P. P.; Maggard, P. A. Crystal Chemistry, Band Engineering, and Photocatalytic Activity of the $LiNb_3O_8$-$CuNb_3O_8$ Solid Solution. *Inorg. Chem.* **2013**, *52*, 4443–4450.

(15) Kato, H.; Takeda, A.; Kobayashi, M.; Hara, M.; Kakihana, M. Photocatalytic Activities of $Cu_{3x}La_{1-x}Ta_7O_{19}$ Solid Solutions for H_2 Evolution under Visible Light Irradiation. *Catal. Sci. Technol.* **2013**, *3*, 3147–3154.

(16) Fukuda, M.; Yamada, I.; Murata, H.; Hojo, H.; Hernandez, O. J.; Ritter, C.; Tanaka, K.; Fujita, K. Perovskite-Type $CuNbO_3$ Exhibiting Unusual Noncollinear Ferrielectric to Collinear Ferroelectric Dipole Order Transition. *Chem. Mater.* **2020**, *32*, 5016–5027.

(17) Sleight, A. W.; Prewltt, C. T. Preparation of $CuNbO_3$ and $CuTaO_3$ at high pressure. *Mater. Res. Bull* **1970**, *5*, 207–211.

(18) Petricek, V.; Dusek, M.; Palatinus, L. Crystallographic Computing System JANA2006: General Features. General features. *Z Krist-Cryst. Mater.* **2014**, *229*, 345–352.

(19) Rodriguez-Carvajal, J. Recent Advances in Magnetic Structure Determination Neutron Powder Diffraction. *Physica B* **1993**, *192*, 55–69.

(20) Kresse, G.; Furthmuller J. Efficiency of Ab-Initio Total Energy Calculations for Metals and Semiconductors Using a Plane-Wave Basis Set. *Comp. Mater. Sci.* **1996**, *6*, 15–50.

(21) Kresse, G.; Furthmuller, J. Efficient Iterative Schemes for Ab Initio Total-Energy Calculations Using a Plane-Wave Basis Set. *Phys. Rev. B* **1996**, *54*, 11169–11186.

(22) Kresse, G.; Joubert, D. From Ultrasoft Pseudopotentials to the Projector Augmented-Wave Method. *Phys. Rev. B* **1999**, *59*, 1758–1775.

(23) Wang, V.; Xu, N.; Liu, J. C.; Tang, G.; Geng, W. T. VASPKIT: A User-Friendly Interface Facilitating High-Throughput Computing and Analysis Using VASP Code. *Comput. Phys. Commun.* **2021**, *267*, 108033.

(24) Perdew, J. P.; Burke, K.; Ernzerhof, M. Generalized Gradient Approximation Made Simple. *Phys. Rev. Lett.* **1997**, *78*, 1396–1396.

(25) Dudarev, S. L.; Botton, G. A.; Savrasov, S. Y.; Humphreys, C. J.; Sutton, A. P. Electron-Energy-Loss Spectra and the Structural Stability of Nickel Oxide: An LSDA+U Study. *Phys. Rev. B* **1998**, *57*, 1505–1509.

(26) Dronskowski, R.; Blochl, P. E. Crystal Orbital Hamilton Populations (COHP). Energy-Resolved Visualization of Chemical Bonding in Solids Based on Density-Functional Calculations. *J. Phys. Chem.* **1993**, *97*, 8617–8624.

(27) Maintz, S.; Deringer, V. L.; Tchougréeff, A. L.; Dronskowski, R. LOBSTER: A Tool to Extract Chemical Bonding from Plane-Wave Based DFT. *J. Comput. Chem.* **2016**, *37*, 1030–1035.

(28) Momma, K.; I. F. VESTA 3 for Three-Dimensional Visualization of Crystal, Volumetric and

Morphology Data. *J. Appl. Crystallogr.* **2011**, *44*, 1272–1276.
(29) Bae, I. T.; Naganuma, H.; Ichinose, T.; Sato, K. Thickness Dependence of Crystal and Electronic Structures within Heteroepitaxially Grown $BiFeO_3$ Thin Films. *Phys. Rev. B* **2016**, *93*, 064115.
(30) Bae, I. T.; Kovács, A.; Zhao, H. J.; Íñiguez, J.; Yasui, S.; Ichinose, T.; Naganuma, H. Elucidation of Crystal and Electronic Structures within Highly Strained $BiFeO_3$ by Transmission Electron Microscopy and First-Principles Simulation. *Sci. Rep.* **2017**, *7*. 46498.
(31) Iyi, N.; Kitamura, K.; Izumi, F.; Yamamoto, J. K.; Hayashi, T.; Asano, H.; Kimura, S. Comparative Study of Defect Structures in Lithium Niobate with Different Compositions. *J. Solid State Chem.* **1992**, *101*, 340–352.
(32) Abrahams, S. C.; Marsh, P. Defect Structure Dependence on Composition in Lithium Niobate. *Acta Chem.* **1986**, *3*, 61–68.
(33) Brese, N. E.; O'keeffe, M. Bond-Valence Parameters for Solids. *Acta Cryst.* **1991**, *47*, 192–197.
(34) Jana, P.; De La Peña O'Shea, V. A.; Montero, C. M.; Gálvez, P.; Pizarro, P.; Coronado, J. M.; Serrano, D. P. Mixed $NaNb_xTa_{1-x}O_3$ Perovskites as Photocatalysts for H_2 Production. *Green Chem.* **2015**, *17*, 1735–1743.
(35) Chen, Z.; Chen, P.; Xing, P.; Hu, X.; Lin, H.; Wu, Y.; Zhao, L.; He, Y. Novel Carbon Modified $KTa_{0.75}Nb_{0.25}O_3$ Nanocubes with Excellent Efficiency in Photocatalytic H_2 Evolution. *Fuel* **2018**, *233*, 486–496.
(36) Zoellner, B.; Stuart, S.; Chung, C. C.; Dougherty, D. B.; Jones, J. L.; Maggard, P. A. $CuNb_{1-x}Ta_xO_3$ ($x \leq 0.25$) Solid Solutions: Impact of Ta(V) Substitution and Cu(I) Deficiency on Their Structure, Photocatalytic, and Photoelectrochemical Properties. *J. Mater. Chem. A* **2016**, *4*, 3115–3126.
(37) Lee, C. W.; Park, H. K.; Park, S.; Han, H. S.; Seo, S. W.; Song, H. J.; Shin, S.; Kim, D. W.; Hong, K. S. Ta-Substituted $SnNb_{2-x}Ta_xO_6$ Photocatalysts for Hydrogen Evolution under Visible Light Irradiation. *J. Mater. Chem. A* **2015**, *3*, 825–831.
(38) Nakada, A.; Kato, D.; Nelson, R.; Takahira, H.; Yabuuchi, M.; Higashi, M.; Suzuki, H.; Kirsanova, M.; Kakudou, N.; Tassel, C.; Yamamoto, T.; Brown, C. M.; Dronskowski, R.; Saeki, A.; Abakumov, A.; Kageyama, H.; Abe, R. Conduction Band Control of Oxyhalides with a Triple-Fluorite Layer for Visible Light Photocatalysis. *J. Am. Chem. Soc.* **2021**, *143*, 2491–2499.
(39) Nakayama, Y.; MacHida, S.; Tsunami, D.; Kimura, Y.; Niwano, M.; Noguchi, Y.; Ishii, H. Photoemission Measurement of Extremely Insulating Materials: Capacitive Photocurrent Detection in Photoelectron Yield Spectroscopy. *Appl. Phys. Lett.* **2008**, *92*, 153306.
(40) Trasatti S. The absolute electrode potential-an explanatory note. *Pure Appl. Chem.* **1986**, *58*, 955–966.
(41) Xu, X.; Wang, R.; Sun, X.; Lv, M.; Ni, S. Layered Perovskite Compound $NaLaTiO_4$ Modified by Nitrogen Doping as a Visible Light Active Photocatalyst for Water Splitting. *ACS Catal.* **2020**, *10*, 9889–9898.
(42) Chen, Y.; Zhao, H.; Liu, B.; Yang, H. Charge Separation between Wurtzite ZnO Polar {001} Surfaces and Their Enhanced Photocatalytic Activity. *Appl. Catal. B* **2015**, *163*, 189–197.
(43) Vonrüti, N.; Aschauer, U. Band-Gap Engineering in $AB(O_xS_{1-x})_3$ Perovskite Oxysulfides: A Route to Strongly Polar Materials for Photocatalytic Water Splitting. *J. Mater. Chem. A* **2019**, *7*, 15741–15748.
(44) Gong, D.; Xu, S.; Zhang, K.; Du, L.; Qiu, P. Enhancing Photoelectrochemical Cathodic Protection Performance by Facile Tuning Sulfur Redox State in Sacrificial Agents. *Chem. Eng. J.* **2022**, *451*, 138552.
(45) Berr, M. J.; Wagner, P.; Fischbach, S.; Vaneski, A.; Schneider, J.; Susha, A. S.; Rogach, A. L.; Jäckel, F.; Feldmann, J. Hole Scavenger Redox Potentials Determine Quantum Efficiency and Stability of Pt-Decorated CdS Nanorods for Photocatalytic Hydrogen Generation. *Appl. Phys. Lett.* **2012**, *100*, 223903.
(46) Zhang, G.; Zhang, W.; Crittenden, J.; Minakata, D.; Chen, Y.; Wang, P. Effects of Inorganic Electron Donors in Photocatalytic Hydrogen Production over $Ru/(CuAg)_{0.15}In_{0.3}Zn_{1.4}S_2$ under Visible Light Irradiation. *J. Renew. Sustain. Energy* **2014**, *6*, 033131.
(47) Xiao, J.; Nishimae, S.; Vequizo, J. J. M.; Nakabayashi, M.; Hisatomi, T.; Li, H.; Lin, L.; Shibata, N.; Yamakata, A.; Inoue, Y.; Domen, K. Enhanced Overall Water Splitting by a Zirconium-Doped TaON-Based Photocatalyst. *Angew. Chem. Int. Ed.* **2022**, *61*, e202116573.
(48) Zhang, B.; Wang, J.; Liu, G.; Weiss, C. M.; Liu, D.; Chen, Y.; Xia, L.; Zhou, P.; Gao, M.; Liu, Y.; Chen, J.; Yan, Y.; Shao, M.; Pan, H.; Sun, W. A Strongly Coupled Ru–CrO_x Cluster–Cluster Heterostructure for Efficient Alkaline Hydrogen Electrocatalysis. *Nat. Catal.* **2024**, *7*, 441–451.
(49) Assimos, J. A.; Trivich, D. Photovoltaic Properties and Barrier Heights of Single-Crystal and Polycrystalline Cu_2O-Cu Contacts. *J. Appl. Phys.* **1973**, *44*, 1687–1693.
(50) Sullivan, I.; Zoellner, B.; Maggard, P. A. Copper(I)-Based p-Type Oxides for Photoelectrochemical and Photovoltaic Solar Energy Conversion. *Chem. Mater.* **2016**, *28*, 5999–6016.
(51) Rajeshwar, K.; Hossain, M. K.; Macaluso, R. T.; Janáky, C.; Varga, A.; Kulesza, P. J. Review—Copper Oxide-Based Ternary and Quaternary Oxides: Where Solid-State Chemistry Meets Photoelectrochemistry. *J. Electrochem. Soc.* **2018**, *165*, 3192–3206.

(52) Fuoco, L.; Joshi, U. A.; Maggard, P. A. Preparation and Photoelectrochemical Properties of P-Type $Cu_5Ta_{11}O_{30}$ and $Cu_3Ta_7O_{19}$ Semiconducting Polycrystalline Films. *J. Phys. Chem. C* **2012**, *116*, 10490–10497.
(53) Ali, S.; Chen, L.; Li, Z.; Zhang, T.; Li, R.; Bakhtiar, S. ul H.; Leng, X.; Yuan, F.; Niu, X.; Zhu, Y. Cu_x-$Nb_{1.1-x}$ (x = 0.45, 0.35, 0.25, 0.15) Bimetal Oxides Catalysts for the Low Temperature Selective Catalytic Reduction of NO with NH_3. *Appl. Catal. B* **2018**, *236*, 25–35.
(54) Paul E. Larson. X-Ray Induced Photoelectron and Auger Spectra of Cu, CuO, Cu_2O, and Cu_2S Thin Films. *J Electron Spectros. Relat. Phenomena* **1974**, *4*, 213–218.
(55) Haber, J.; Machej, T.; Ungier, L.; Zidekowski, J. ESCA Studies of Copper Oxides and Copper Molybdates. *J. Solid State Chem.* **1978**, *25*, 207–218.
(56) Pauly, N.; Tougaard, S.; Yubero, F. Determination of the Cu 2p Primary Excitation Spectra for Cu, Cu_2O and CuO. *Surf. Sci.* **2014**, *620*, 17–22.
(57) Butler, M. A.; Ginley, D. S., Prediction of Flatband Potentials at Semiconductor-Electrolyte Interfaces from Atomic Electronegativities. *J. Electrochem. Soc.* **1978**, *125*, 228–232.
(58) McClarin, G. R.; Berger, R. F. Confluence of Structural Distortion and A-Site Composition in the Band Gaps of Perovskite Niobate and Tantalate Photocatalysts. *Phys. Rev. B* **2019**, *100*, 045202.

Table of Contents artwork